



# Heat transfer effect on the modeling of jets under supercritical and transcritical conditions

Leandro B. Magalhães<sup>1,2</sup> · André R. Silva<sup>2</sup> · Jorge M. Barata<sup>2</sup>

Received: 2 August 2023 / Revised: 21 December 2023 / Accepted: 30 December 2023  
© The Author(s) 2024

## Abstract

The injection of nitrogen under supercritical and transcritical conditions, where the injection temperature is below nitrogen's critical point, but the pressure is above it, is considered in this paper. While the scientific community recognizes that the sharp gradients of the different thermophysical parameters make it inappropriate to employ a two-phase flow modeling at conditions above the critical point, the issue is not restrained to the mere representation of turbulence for a mono-phase flow. Instead, a quantitative similarity with gas-jet-like behavior led to proposing an incompressible but variable density hypothesis suitable for describing supercritical and sub/near-critical conditions. Presently, such an approach is extended and assessed for a configuration including injector heat transfer. As such, axial density and temperature decay rates and jet spreading rates of density and temperature are evaluated, indicating a higher mixing efficiency in the supercritical regime and an overall dominance of heat propagation over momentum transport, with a greater preponderance in the supercritical regime.

**Keywords** Transcritical mixing · Supercritical mixing · Liquid rocket engines

## 1 Introduction

The efficiency of any given rocket engine can be estimated from the specific impulse as defined in equation (1), where  $I_{sp}$  is the specific impulse,  $g$  the gravitational acceleration,  $\gamma$  the adiabatic index,  $\mathcal{R}$  the ideal gas constant,  $p_e$  the nozzle exit pressure and  $T_\infty$  and  $p_\infty$  the chamber temperature and pressure, respectively.

$$I_{sp} = \frac{1}{g} \left[ \frac{2\gamma\mathcal{R}T_\infty}{\gamma-1} \left( 1 - \left( \frac{p_e}{p_\infty} \right)^{\frac{\gamma-1}{\gamma}} \right) \right]^{0.5} \quad (1)$$

Liquid rocket engine (LRE) performance is greatly influenced by propellant mixing near the injectors [1–7]. Equation (1) indicates that besides adjusting the fuel-to-oxidizer ratio (which leads to a change in temperature and isotropic coefficient), the only option remaining to increase the specific impulse is to raise the engine operating pressure and temperature, leading mixtures to transcritical and supercritical regimes. Also, in turbine engines, the increase in inlet temperature and operating pressure, with a given exit pressure, lead to improvements in engine performance [8]. The application of supercritical fluids in propulsive systems such as rockets or jet engines is not restricted to the pursuit of higher power conversion rates since the high thermal loads need to be mitigated through regenerative cooling systems [9–11].

The supercritical regime is defined by pressure and temperature above their critical point values, as depicted in Fig. 1. It is a thermodynamic singularity where mass diffusivity, surface tension, and latent heat are zero. In contrast,

---

Leandro B. Magalhães, André R. Silva and Jorge M. Barata have contributed equally to this work.

✉ Leandro B. Magalhães  
leandro.magalhaes@iseclisboa.pt

André R. Silva  
andre@ubi.pt

Jorge M. Barata  
jbarata@ubi.pt

<sup>1</sup> Aeronautics Department, Higher Institute for Education and Sciences, Alameda das Linhas de Torres 179, 1750-142 Lisboa, Portugal

<sup>2</sup> Aerospace Sciences Department, AEROG-LAETA, Universidade da Beira Interior, Calçada Fonte do Lameiro, 6, 6200-358 Covilhã, Portugal

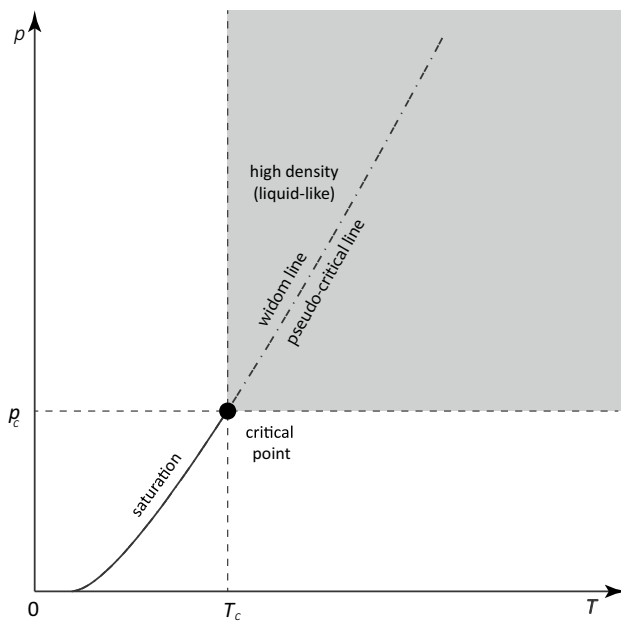


**Fig. 1** Overall pressure-temperature diagram

isentropic compressibility, specific heat, and thermal conductivity tend to infinity. Moreover, the distinction between liquid and gas phases disappears due to the absence of surface tension. In the case of pure fluids, critical pressure and temperatures work as identifiers of the fluid. In contrast, in the case of multi-species mixtures, the critical point assumes a dynamic nature depending on the amount of each species in the mixture at any given moment, and critical mixing lines are instead defined [12]. Due to the non-linear behavior of the different thermophysical parameters at and around the critical point, the fluid will have liquid-like density and gas-like properties [13]; mass diffusion will replace vaporization as the governing parameter, and diffusion will dominate over the jet atomization process.

By combining pressure and temperature values above and below the critical point, in Fig. 1, three more regimes can be defined: subcritical, transcritical, and superheated. Since the transcritical regime is characterized by temperatures lower than the critical value, the formation of two-phase flow and phase separation is a reality. Considering pressure and temperature values below the critical point, the subcritical regime is defined, where the commonly known primary and secondary breakup occurs, and the liquid–gas discontinuity happens. While the coexistence line ends at the critical point, the Widom line extends in the supercritical regime, separating supercritical liquid-like from gas-like regimes [14], assuming the moniker Widom or pseudocritical line.

This continuous non-equilibrium process occurs within a narrow temperature range in opposition to transition at subcritical conditions. Later, it would be demonstrated [15] that the Widom line denotes a fundamental change in jet breakup from the dominance of mechanical breakup to a thermal breakup process which could even happen inside the injector [15] provided that the flow received enough heat to trigger the pseudo phase change. Then the role of thermal breakup introduced by Banuti and Hannemann [15] would be confirmed through direct numerical simulation (DNS) [16] and the comparison extended to a broader range of conditions [17].

While the distinction between liquid and transcritical states is not based on any physical arguments [18], the term transcritical commonly refers in the literature to a fluid with a temperature below the critical point condition and pressure above it, leaving the moniker subcritical reserved for the description of fluid with pressure and temperature below critical point values. As a result, it is natural to hypothesize that similarities can be found between both regimes. In this sense, several experimental measurements [1, 19–21] provide quantitative arguments in favor of the variable-density nature of supercritical jets, being similar descriptions encountered for diesel injection [22]. Typically these experiments are conducted at relatively constant pressure, resulting in the dependency of the density gradient solely on temperature, effectively considering density incompressible or weakly compressible. Here, compressibility effects are understood as changes in pressure induced by volumetric changes. Studies on the effects of compressibility on high-pressure injection systems [23] indicate how fuel density affects jet evolution [7, 24]. Furthermore, the low injection velocity at which the experiments are conducted, allied with considering real gas properties, allows for employing incompressible solution schemes while considering the variable-density behavior of supercritical fluids. Recently the incompressible but variable density approach was used to model supercritical injection [17], leaving its suitability to the description of transcritical injection as an open question. In the same way as in Magalhães et al. [17], the mechanical versus thermal breakup proposed by Banuti and Hannemann [15] is used to evaluate the role of injector heat transfer, particularly in the transcritical regime. In the present work, an incompressible but variable density approach [25] is used to model the mixing behavior of a fluid injected at supercritical and transcritical conditions into a quiescent supercritical environment [20] as representative of the pressure and temperature conditions in the combustion chamber of a liquid rocket engine. Here the term liquid rocket engine refers to rocket engines using fuel and oxidizers stored at very low temperatures. While the scientific community recognizes that employing two-phase flow approaches is

unsuitable for describing flows at supercritical conditions, the issue is open to more than just a single-phase representation of turbulence. Chehroudi et al. [26] measurements highlighted a quantitative similarity between supercritical and gas-jet-like jet behavior. This led to the hypothesis that computational methods used for gaseous jets could be extended to the supercritical regime [25].

Interestingly, no droplets and ligaments are observed, and transition cannot be easily predicted since the critical points of the species in the mixture cannot be used directly [27]. Additional experiments conducted by Segal and Polikhov [28] corroborate the decreased importance of surface tension at transcritical conditions and jet breakup in the form of detached finger-like structures. As described by Oschwald and Schik [20], the importance of surface tension lies in the fact that in rocket combustors, there is no thermal equilibrium, and surface tension varies locally, as does the mixture critical point. Given the highly coupled phenomena, traditional experimental techniques experience difficulty reporting the characteristic of dense sprays due to the variable density conditions.

The question then becomes how to model the behavior of fluids under the influence of such highly coupled phenomena. Recent extensive reviews on transcritical flows were put together by Jofre and Urzay [29] and Ries and Sadiki [30]. Concepts such as partial-mass and partial-density were proposed [31] to be used to treat a fluid flow over the relevant thermodynamic states. Moreover, Sierra-Pallares et al. [32] analyzed nitrogen mixing layers at transcritical and supercritical conditions through Reynolds-averaged Navier–Stokes (RANS), following a mixture fraction formulation, while Tao et al. [33] proposed a low-Reynolds turbulence model correction to replicate supercritical hydrocarbon behavior in a round pipe. These studies present important insights to the field, but do not indicate the effect injector heat transfer has on transcritical jets. So, in the present work, the incompressible but variable approach is further used to improve the knowledge of the supercritical and transcritical jet characteristics in a quiescent supercritical environment as representative of the pressure and temperature conditions in the combustion chamber of a liquid rocket engine. In the present work such an approach is extended and assessed for a configuration including injector heat transfer with application to rocket engines.

The remainder of this paper is divided into four sections: first, the incompressible but variable density formulation is summarized with the methods employed to describe the thermophysical parameters. Then the experimental test cases are presented and discussed. Results are finally discussed, focusing on axial density, temperature decay, and injection spreading rates. Lastly, the main findings are reported in the conclusions.

## 2 Mathematical formulation

The flow is modeled through an incompressible but variable density approach as described by Magalhães [34], where all the employed models are fully described, being only a general description of the flow modeling is given here.

The Favre-averaged conservation equations for mass, momentum, and energy are given by equations (2) to (4), respectively, where  $i$  and  $j$  are the directional vectors,  $\rho$  is the density,  $u$  the velocity,  $p$  the pressure,  $\tau$  the viscous stress tensor,  $q$  the heat flux and  $h$  the enthalpy.

$$\frac{\partial \bar{u}_i}{\partial x_i} = 0 \quad (2)$$

$$\frac{\partial \bar{u}_i \bar{u}_j}{\partial x_j} = -\frac{\partial \bar{p}}{\partial x_i} + \frac{\partial \bar{\tau}_{ij}}{\partial x_j} - \bar{\rho} \frac{\partial \widetilde{u_i' u_j'}}{\partial x_j} \quad (3)$$

$$\begin{aligned} \frac{\partial \bar{u}_j \bar{H}}{\partial x_j} &= \frac{\partial \bar{\tau}_{ij} u_i}{\partial x_j} \\ &- \bar{\rho} \frac{\partial \widetilde{u_i' u_j' h''}}{\partial x_j} - \frac{\partial \bar{q}_j}{\partial x_j} + \bar{\rho} \frac{\partial \widetilde{u_j' h''}}{\partial x_j} \end{aligned} \quad (4)$$

The Reynolds stress tensor and turbulence heat flux are evaluated from equations (5) and (6), respectively, where  $k$  represents the turbulence kinetic energy,  $\delta$  the Kronecker's delta function,  $\mu_t$  the eddy viscosity,  $c_p$  the isobaric-specific heat,  $T$  the temperature and  $\text{Pr}_t$  the turbulent Prandtl number.

$$\begin{aligned} \bar{\rho} \widetilde{u_i' u_j'} &= -\frac{2}{3} \rho k \delta_{ij} \\ &+ \mu_t \left( \frac{\partial \bar{u}_i}{\partial x_j} + \frac{\partial \bar{u}_j}{\partial x_i} - \frac{2}{3} \frac{\partial \bar{u}_k}{\partial x_k} \delta_{ij} \right) \end{aligned} \quad (5)$$

$$\begin{aligned} \bar{\rho} \widetilde{u_j' h''} &= -\frac{c_p \mu_t}{\text{Pr}_t} \\ \frac{\partial \bar{T}}{\partial x_j} &= -\frac{\mu_t}{\text{Pr}_t} \frac{\partial \bar{h}}{\partial x_j} \end{aligned} \quad (6)$$

The system of partial differential equations (PDE) is closed with the standard  $k$ - $\epsilon$  turbulence model [35] introducing two new field equations, one for the turbulence kinetic energy and another for its dissipation. Eddy viscosity is evaluated from equation (7), while turbulence kinetic energy and its dissipation rate are evaluated from equations (8) and (9), respectively. The model constants used are  $\sigma_\kappa = 1.0$ ,  $\sigma_\epsilon = 1.3$ ,  $C_\mu = 0.09$ ,  $C_{\epsilon 1} = 1.35$ ,  $C_{\epsilon 2} = 1.8$  and  $f_1 = 1.0$ . The turbulence closure choice arose from a previous study [36], where several RANS-based closure formulations were compared, ranging from simple eddy viscosity to second-order

closures. Similar comparisons were carried out in the context of LES [37] to assess the suitability of sub-grid scale (SGS) models, yielding similar conclusions.

$$\mu_t = C_{\mu} f_{\mu} \frac{\rho \kappa^2}{\epsilon} \quad (7)$$

$$\frac{\partial(\rho u_j \kappa)}{\partial x_j} = P - p\epsilon + \frac{\partial}{\partial x_j} \left[ \left( \mu + \frac{\mu_t}{\sigma_{\kappa}} \right) \frac{\partial \kappa}{\partial x_j} \right] \quad (8)$$

$$\begin{aligned} \frac{\partial(\rho u_j \epsilon)}{\partial x_j} &= C_{\epsilon 1} f_1 \frac{\epsilon}{\kappa} P - C_{\epsilon 2} f_2 \frac{\rho \epsilon^2}{\kappa} \\ &+ \frac{\partial}{\partial x_j} \left[ \left( \mu + \frac{\mu_t}{\sigma_{\epsilon}} \right) \frac{\partial \epsilon}{\partial x_j} \right] \end{aligned} \quad (9)$$

The Peng-Robinson [38] equation of state was used to compromise computational affordability and result accuracy [39]. It is given following equation (10), with  $v$  being the specific volume and  $a$  and  $b$  representing attractive (equation (11)) and repulsive potentials (equation (12)). Parameter  $\alpha$  is retrieved following equations (13) and (14) dependent upon the acentric factor ( $\omega$ ), where subscript  $c$  respects critical point property and  $r$  a reduced property.

$$p = \frac{RT}{v-b} - \frac{a\alpha(T)}{v(v+b) + b(v-b)} \quad (10)$$

$$a = \frac{0.45724R^2T_c^2}{P_c} \quad (11)$$

$$b = \frac{0.0778RT_c}{P_c} \quad (12)$$

$$\alpha = [1 + k(T_r^{1/2})]^2 \quad (13)$$

$$k = 0.37464 + 1.54226\omega - 0.26992\omega^2 \quad \omega \leq 0.49 \quad (14)$$

The representation of any given thermodynamic property could be derived for a thermodynamic potential such as enthalpy as a sum of ideal gas properties added to a departure function to account for the real gas behavior in what is commonly referred to as a thermal equation of state, given according to equation (15). The ideal gas enthalpy is given by the seven-coefficient NASA polynomials [40]. In contrast, the real gas contribution is derived from the Peng and Robinson [38] equation of state (equation (10)), explicitly

defined in equation (16), with parameter  $\alpha$  variation with temperature defined in equation (17).

$$h(p, T) = h_0(T) + \int_{p_0}^p \left[ \frac{1}{\rho} + \frac{T}{\rho^2} \left( \frac{\partial p}{\partial T} \right)_{\rho} \right] dp \quad (15)$$

$$\begin{aligned} \frac{h(p, T) - h_0(T)}{R} &= \frac{a\alpha(T) \frac{\partial \alpha}{\partial T}}{RT \sqrt{8b^2}} \\ &\ln \left( \frac{2v + 2b - \sqrt{8b^2}}{2v + 2b + \sqrt{8b^2}} \right) - 1 + Z \end{aligned} \quad (16)$$

$$\frac{\partial \alpha}{\partial T} = -\frac{k\alpha(T)}{T_c T_r^{1/2}} \quad (17)$$

Similarly, transport properties such as thermal conductivity and dynamic viscosity are represented following the departure function formalism [41] where a departure function is added to account for the real gas effect to the ideal gas property.

From a numerical standpoint, a finite volume method is used where diffusive terms are discretized following the second-order central schemes. In contrast, advective ones follow the third-order accurate QUICK scheme [42], which helps mitigate the appearance of spurious pressure oscillations due to the equation of state solving and the transition across the Widom line. Following Jarczyk and Pfitzner [43], a pressure evolution equation is used, obtained from the divergence in the momentum (equation (3)). As detailed by Müller et al. [44], pressure- and density-based formulation yielded similar predictions in terms of mean axial density decays for supercritical nitrogen mixing layers.

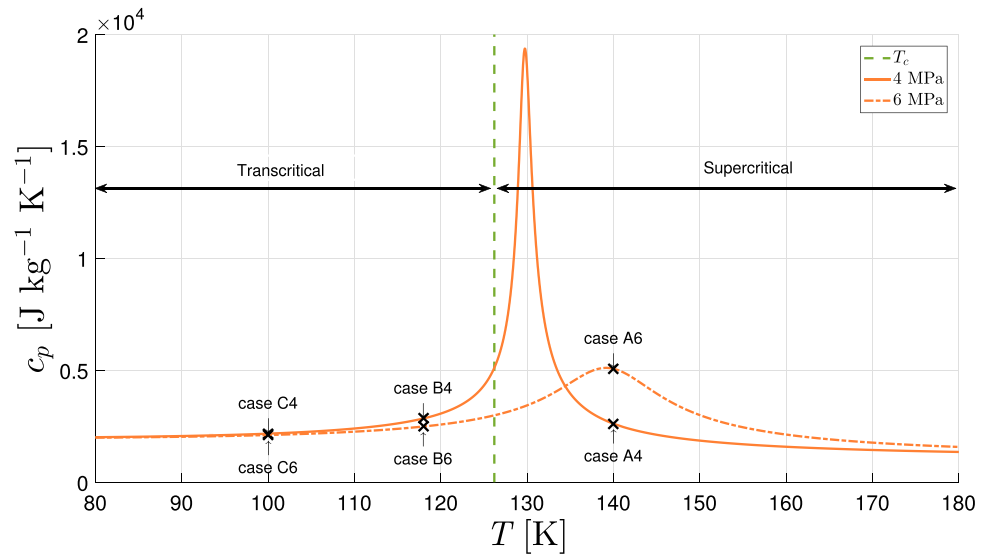
### 3 Review of the experiment

The experiment carried out by Oswald and Schik [20], at quasi-isobaric conditions of nitrogen's injection under supercritical and transcritical conditions is used to validate the numerical results hereby presented. Table 1 details parameters such as injection velocity and temperature for pressures of 4 and 6 MPa, depicted in Fig. 2.

The velocity at injection,  $v_{inj}$ , varies from 5 m s<sup>-1</sup>, for cases A and B to 20 m s<sup>-1</sup> in cases C. This variable is calculated from the measured mass flux. Moreover, the injection temperature of cases A4 and A6 is 140 K for, while in cases B4 and B6 it assumes the value of 118 K. In contrast, an even lower temperature of 100 K is taken for transcritical jet cases C4 and C6. The temperature inside the chamber is kept

**Table 1** Summary of the experimental conditions [20]

case	$p_\infty$ [MPa]	$v_{inj}$ [m s <sup>-1</sup> ]	$T_{inj}$ [K]	$T_\infty$ [K]	$\rho_{inj}$ [kg m <sup>-3</sup> ]	$\rho_\infty$ [kg m <sup>-3</sup> ]
A4	4.0	5.0	140	298	150.06	45.39
B4	4.0	5.0	118	298	583.02	45.39
C4	4.0	20.0	100	298	706.82	45.39
A6	6.0	5.0	140	298	338.13	68.03
B6	6.0	5.0	118	298	608.94	68.03
C6	6.0	20.0	100	298	716.43	68.03

**Fig. 2** Location of the experimental test cases concerning the critical point of nitrogen**Table 2** Non-dimensional evaluations [20]

case	$p_\infty/p_c$	$T_{inj}/T_c$	$\rho_{inj}/\rho_\infty$
A4	1.17	1.11	3.34
B4	1.17	0.94	12.5
C4	1.17	0.79	15.7
A6	1.76	1.11	5.01
B6	1.76	0.84	8.99
C6	1.76	0.79	10.6

constant at 298 K through the use of electrical heating [20]. Increasing the pressure in the flow channel from 4 to 6 MPa increases the density of the reservoir gas and, simultaneously, significantly alters the thermodynamic behavior of the cryogenic nitrogen.

Table 2 shows reduced pressure and temperature, and the density ratio between the injection condition and the combustion chamber, making it possible to easily identify which condition does one particular jet configuration corresponds to – transcritical or supercritical.

The experimental setup is represented in Fig. 3. The injector and chamber have diameters of 1.9 mm and 100 mm, respectively. While the chamber has a total length of 1 m, only 250 mm are considered in order to decrease the computational cost while ensuring the domain is large enough so

that the outlet conditions do not affect the region of interest. Lastly, the length of the injector is considered to be 90 mm.

Velocities and temperatures are imposed at the inlet, according to Table 1, with a gauge pressure of 0 MPa imposed at the outlet. In addition, isothermal wall boundary conditions are applied to the injector with imposed values of 298 K [15] and chamber walls. Finally, an adiabatic condition is used for the chamber faceplate.

## 4 Validation

Figures 4 and 5 depict grid sensitivity analysis for test cases A4 and B4, representing the two distinct regimes considered – transcritical and supercritical injection conditions. As can be observed minimal slope variation was encountered for the mean axial density decay of the each considered mesh: a refined mesh with 480 537, an intermediate one having 252 459 points and a coarse one with 182 988 points. Moreover wall functions are used, due to the standard  $\kappa - \epsilon$  turbulence model employment. As such a  $y^+$  value of 11.63 is ensured for the first grid cell close to the solid boundaries. Density is depicted as the ratio between the axial density decay and the initial

**Fig. 3** Boundary Conditions corresponding to the experimental conditions of Oswald and Schik [20]

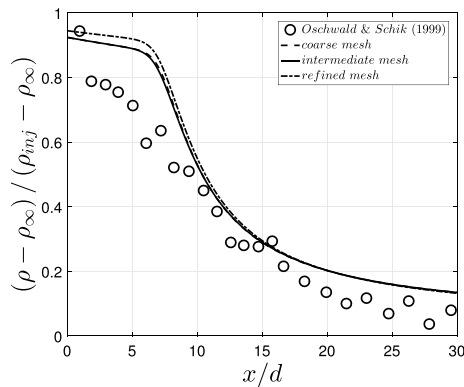
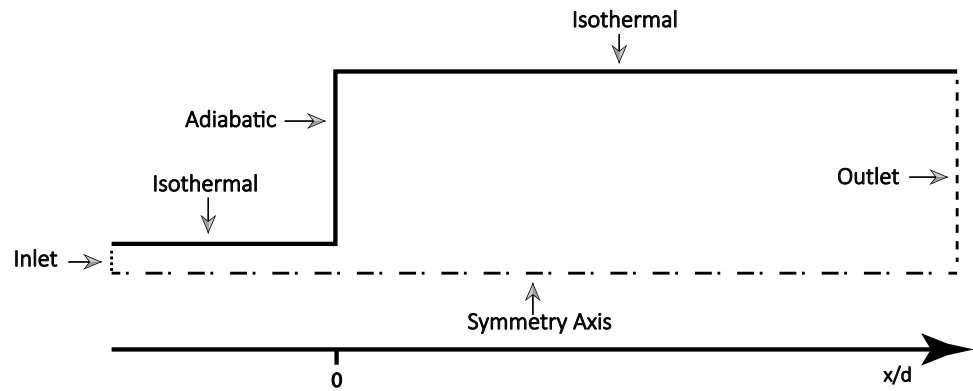


**Fig. 4** Grid independence study for supercritical case A4

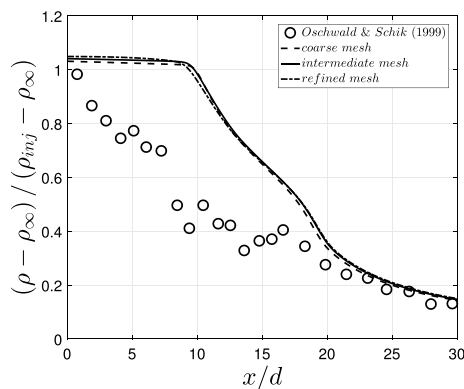


**Fig. 5** Grid independence study for transcritical case B4

density as a function of the normalized axial distance to the injector diameter.

In Fig. 6, a representation of the error as a function of the grid convergence index [45] (CGI) indicates how the numerical error decreases as the grids are progressively refined, exhibiting a slope steeper than second-order.

## 5 Results

Figure 7 compares the computations and the experimental data [20]. In the top figure, nitrogen's non-dimensional axial density decay ( $\rho^*$ ) is represented, defined according to equation (18). The middle figure represents the full width at half maximum (FWHM) of density, which measures the jet spreading rate. Since the shear layer's edge is difficult to obtain from Raman scattering [46], the FWHM is calculated instead. Lastly, the bottom figure represents the shape parameter,  $n_\rho$  for density, evaluated from equation (19) [47], giving a measure of the axial density shape profile. Axial density, FWHM of density, and shape parameter are evaluated as a function of the non-dimensional distance from the injector exit plane,  $x/d$ . In (19), the  $n$  describes the dependence with the radial velocity component, while  $r_m$  is the radial position at which the profile reaches its half-value.

$$\rho^* = \frac{\rho - \rho_\infty}{\rho_{inj} - \rho_\infty} \quad (18)$$

$$f\left(\frac{r}{r_m}\right) = \tanh^2 \left[ 0.881 \left(\frac{r}{r_m}\right)^n \right] \quad (19)$$

Furthermore, Oswald and Schik [20] use the NIST [48] database to convert the density profiles into temperature ones, which can be achieved, for instance, through Fig. 2. Accordingly, Fig. 8 depicts the axial temperature decay, FWHM of temperature, and the temperature shape parameter, being the non-dimensional temperature ( $T^*$ ) defined following equation (20).

$$T^* = \frac{T - T_\infty}{T_{inj} - T_\infty} \quad (20)$$

From Fig. 2, it is easy to identify case A4, depicted in Figs. 7 and 8 for density- and temperature-related parameters as corresponding to supercritical gas-like conditions, exhibiting the subsided core identified in Banuti and Hannemann [15]



**Fig. 6** Comparison of grid independence study with Richardson's interpolation

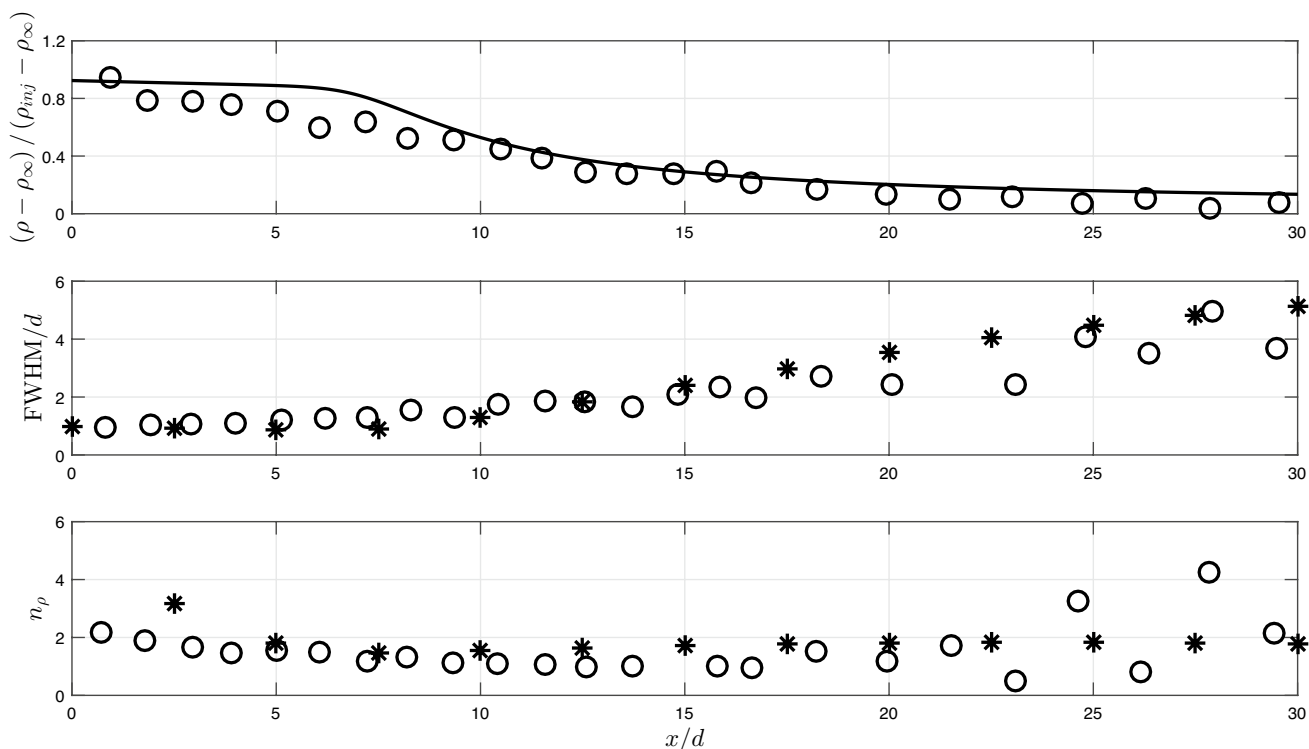
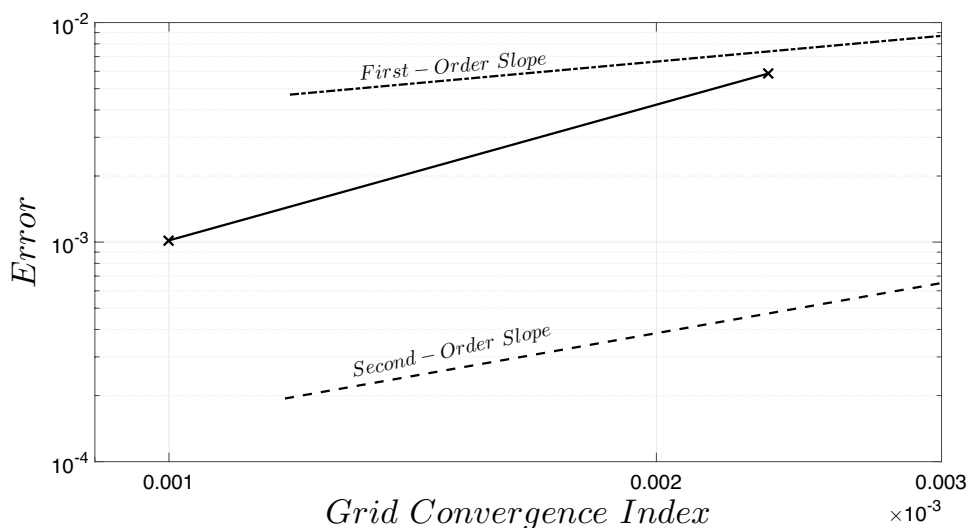


**Fig. 7** Comparison between numerical results and experimental results for case A4 (top: axial density distribution; middle: FWHM of density; bottom: shape parameter). Lines and star symbols correspond to numerical results, while open circles represent experimental data [20]

up to an axial distance of 7 injector diameters. Then, entrainment from the lower-density chamber nitrogen into the jet increases the axial decay rate.

Looking at the axial temperature distribution, it is possible to observe a similar trend as the one found for the axial density distribution. A low rate of temperature decay is seen until  $x/d \approx 7$ , after which it increases to  $x/d \approx 18$ . After this

point, a higher temperature value is retrieved concerning the one obtained by Oschwald and Schik [20].

A similar behavior is encountered in the higher pressure configuration case A6 (Figs. 9 and 10). Here the subsided core extends up to a distance of 8 injector diameters owing to the large density gradients between injection and

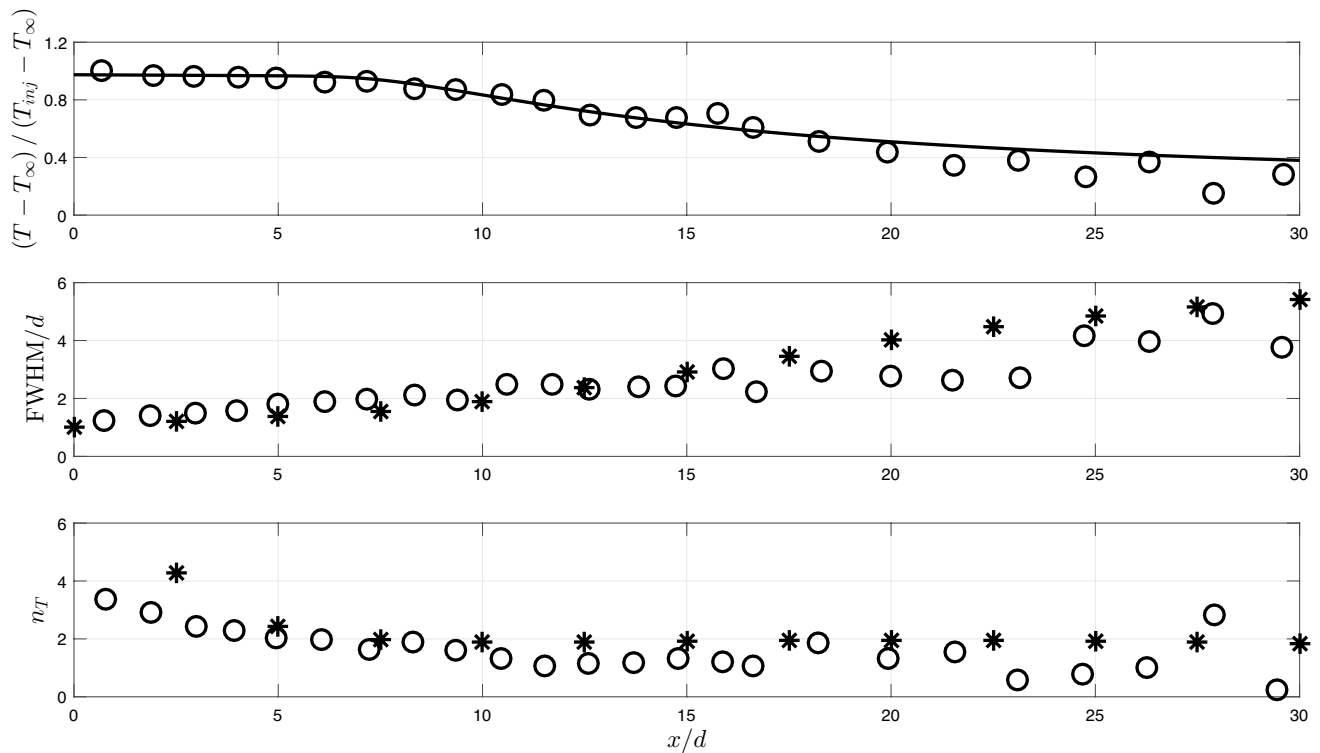


**Fig. 8** Comparison between numerical results and experimental results for case A4 (top: axial temperature distribution; middle: FWHM of temperature; bottom: shape parameter). Lines and star symbols correspond to numerical results, while open circles represent experimental data [20]

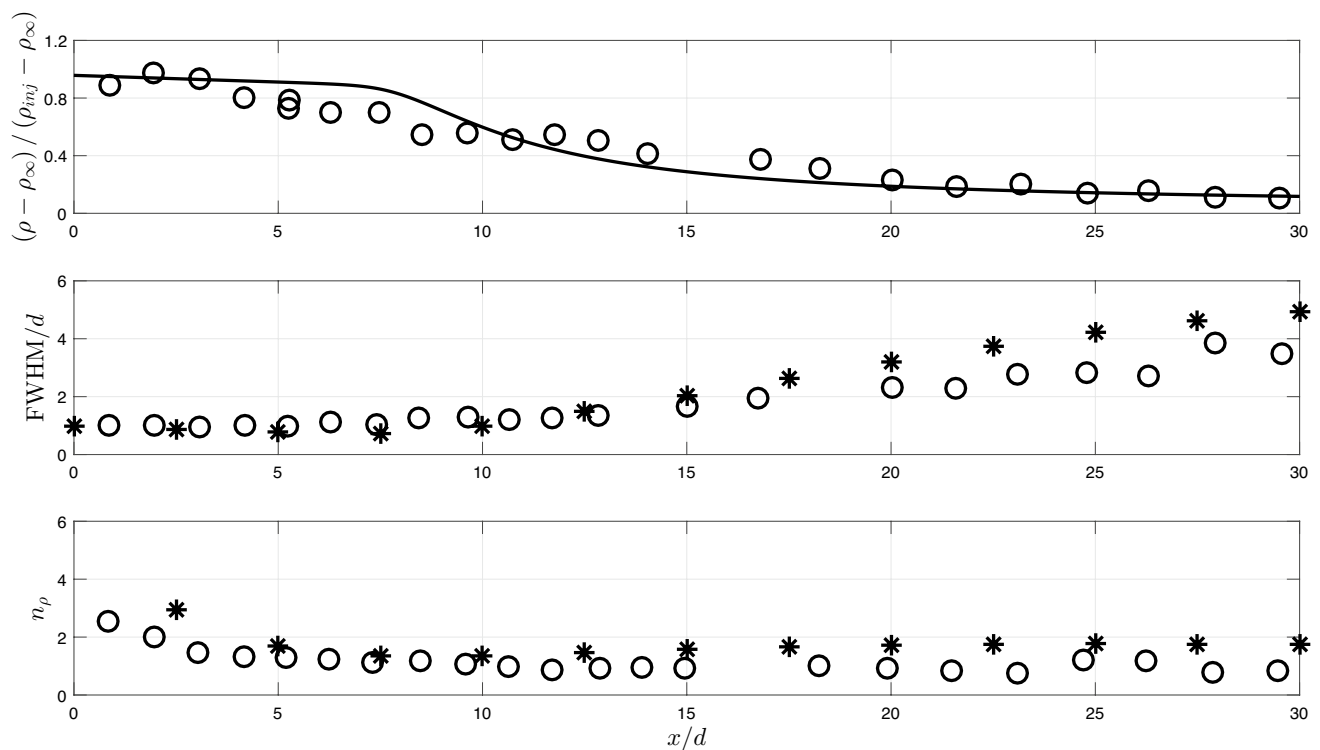


**Fig. 9** Comparison between numerical results and experimental results for case A6 (top: axial density distribution; middle: FWHM of density; bottom: shape parameter). Lines and star symbols correspond to numerical results, while open circles represent experimental data [20]



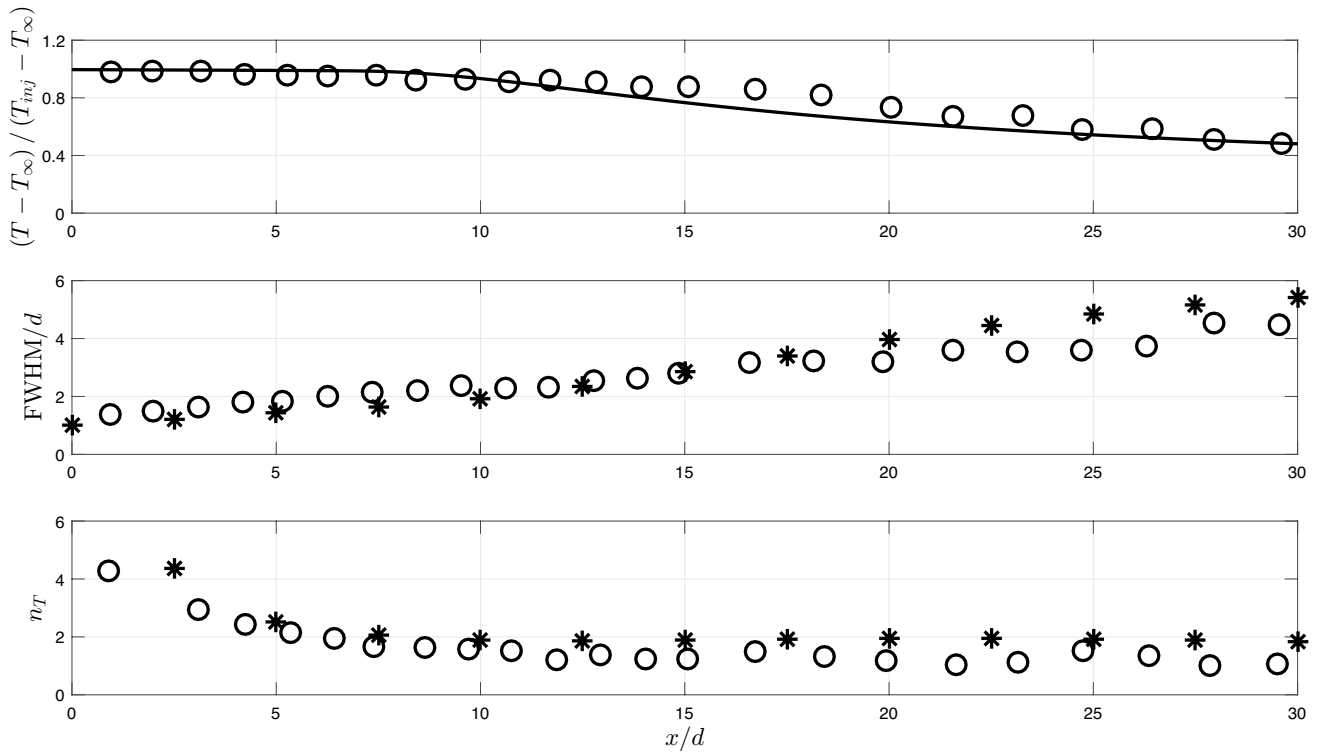


**Fig. 10** Comparison between numerical results and experimental results for case A6 (top: axial temperature distribution; middle: FWHM of temperature; bottom: shape parameter). Lines and star symbols correspond to numerical results, while open circles represent experimental data [20]

chamber conditions. Then, axial density starts to decay faster due to nitrogen entrainment into the jet.

Worthy of note is also the fact that case A6 is located very close to the peak in isobaric-specific heat (Fig. 2), which according to the analysis carried out in Banuti and Hannemann [15] would correspond to the appearance of a plateau-type core. However, it is not the case since a sloped core is depicted. For convenience, the position

of case A6 concerning the peak in isobaric-specific heat is reminded in Fig. 11, alongside cases 5, 6, 9, and 10 from Mayer et al.[21], while experimental chamber and injection conditions are compared in Table 3. Here, chamber pressure conditions and the measured injection temperatures are comparable between the different cases. However, the injection velocities are not.

**Fig. 11** Location of several experimental test cases about the peak in isobaric-specific heat. Cases 5, 6, 9, and 10 from Mayer et al. [21] and case A6 from Oswald and Schik [20]

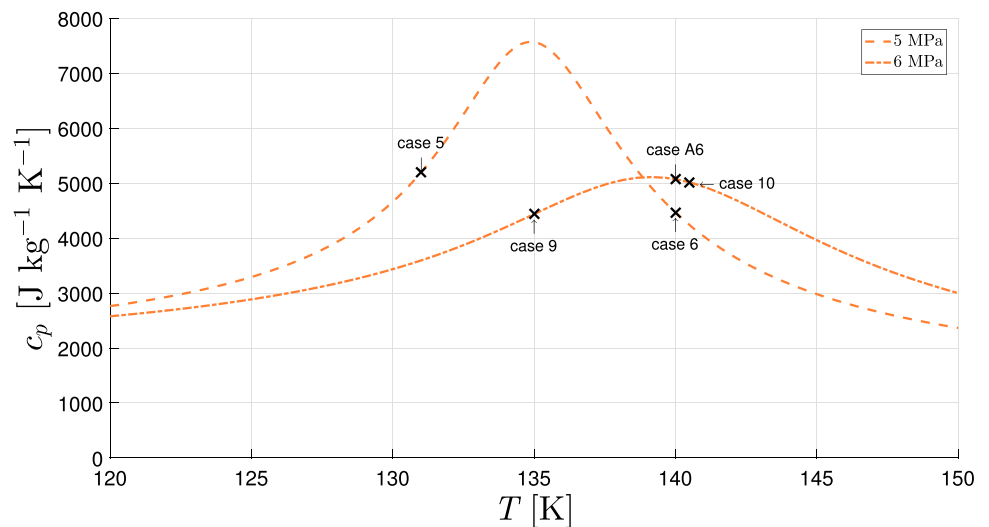


**Table 3** Location of several experimental test cases concerning the peak in isobaric-specific heat. Cases 5, 6, 9, and 10 from Mayer et al. [21] and case A6 from Oswald and Schik [20]

Case	Calculated Velocity [m s <sup>-1</sup> ]	Measured Chamber Pressure [MPa]	Measured Temperature [K]
5	2.0	4.90	131.0
6	1.9	4.90	140.0
9	2.0	5.85	135.0
10	1.9	5.88	140.5
A6	5.0	140.0	

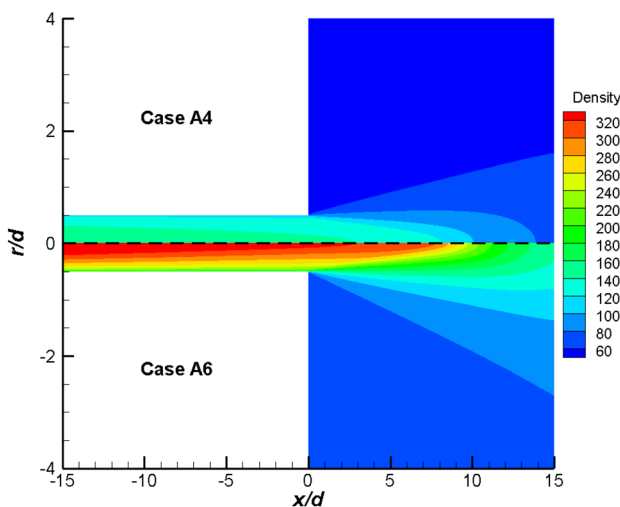


**Fig. 12** Comparison of density field between cases A4 and A6

Compared to Mayer et al. [21] cases, in A6 [20], the injection velocity is more than twice that of the other cases, which can be responsible for the formation of a subsided core instead of a plateau-type core. It is therefore hypothesized that in proximity to the maxima in isobaric-specific heat, the nitrogen jet is more easily entrained by the chamber fluid in the cases of lower injection velocities, leading to intermediate regions forming constant density until entrainment is so vigorous that the core breaks down completely. Here more experimental data would be needed to validate the proposed hypothesis and unravel the limits in which each core type is formed.

As depicted in Fig. 12, a comparison between cases A4 and A6 density fields, highlighting the injection and the near field region, indicates that both jets have similar developments, albeit with distinct values of injection density. Fundamentally, in the injection portion of the field, it is possible to observe the density stratification leading to the subsided core [15] appearance in the axial decay rate.

Mean axial centerline decay rates of density and temperature are depicted in Figs. 13 and 14, respectively, for

experimental test case B4. Here, the experimental jet exhibits a fluctuating behavior up to an axial distance from the injector's exit plane of 10 diameters, promoting entrainment. In terms of temperature, a closer agreement is observed with the experimental data due to the lower gradients in relation to density. On the other hand, numerically, the jet develops at a much lower density decay rate to a distance of approximately 9.8 injector diameters. Then the critical temperature value is reached for a normalized density of  $\rho^* = 0.9544$ . Comparing the experimental and numerical results in terms of the mean quantities decay rates, it is observed that the experimental trend is not numerically replicated. Nonetheless, looking at the FWHM values, a good approximation of the experimental data is obtained. It increases at an  $x/d \approx 10$ , consistent with the higher mixing ratio characteristic supercritical conditions.

Similarly to case B4, density- and temperature-related parameters of case B6 in Figs. 15 and 16 exhibit the same trends albeit at a higher density ratio between injection and chamber conditions. The distinct initial behavior between experiments and numerical computations is evident until the transcritical jet reaches nitrogen's critical temperature.

At transcritical conditions (cases B4 and B6), future work will look into how transcritical (temperature below the critical point and pressure above it) jet behavior can be incorporated into the proposed computational framework. Nevertheless, jet growth rates at supercritical and transcritical conditions are satisfactorily replicated in terms of density and temperature, indicating higher mixing rates at supercritical conditions and a preponderance of temperature effects. Accordingly, Fig. 17 depicts higher density stratification inside the injector for case B4 than B6, which verifies the existence of more significant density gradients closer to nitrogen's critical pressure. To the author's best knowledge, it is the first time thermal stratification has been shown to affect transcritical jet conditions. This observation is accord with the pioneering work carried out by Banuti and Hanneemann [15] and seems to suggest that jets at transcritical and supercritical liquid-like conditions are subjected to the same mechanical breakup mechanism. While thermal breakup [15] dictates supercritical gas-like jet breakup. Moreover, thermal stratification directly impacts the operation of LRE due to the role potential core length has in the development of combustion instabilities [49, 50].

Progressively increasing the computational injection temperature of case B4 from the experimental value of 118 K, to 125 K and 128 K several different features can be observed in Fig. 18. In reduced temperature these injection conditions are evaluated from Table 4.

Approaching the critical temperature, we can observe, by taking into account injection temperatures of 118 K and 125 K, density's rate of decay decreases even further for the first section ( $x/d \approx 9.8$ ) for both conditions, while

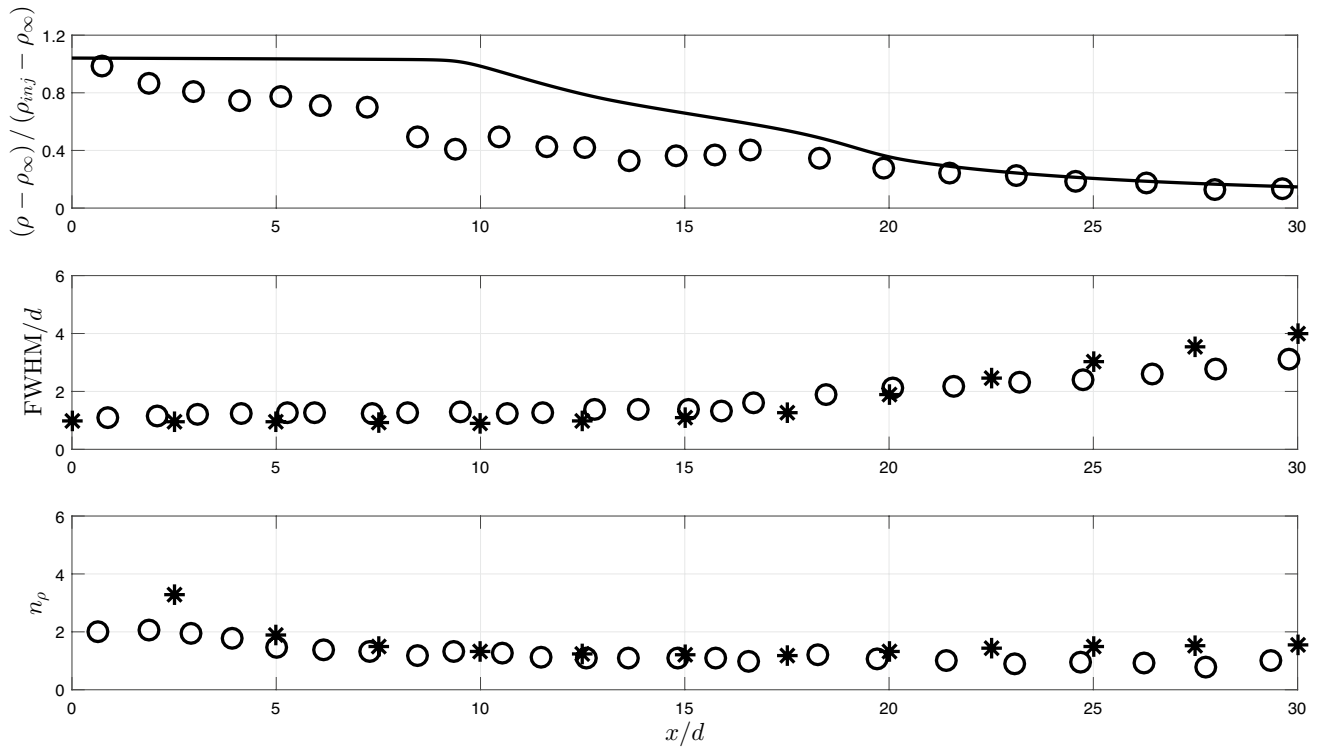


**Fig. 13** Comparison between numerical results and experimental results for case B4 (top: axial density distribution; middle: FWHM of density; bottom: shape parameter). Lines and star symbols correspond to numerical results, while open circles represent experimental data [20]

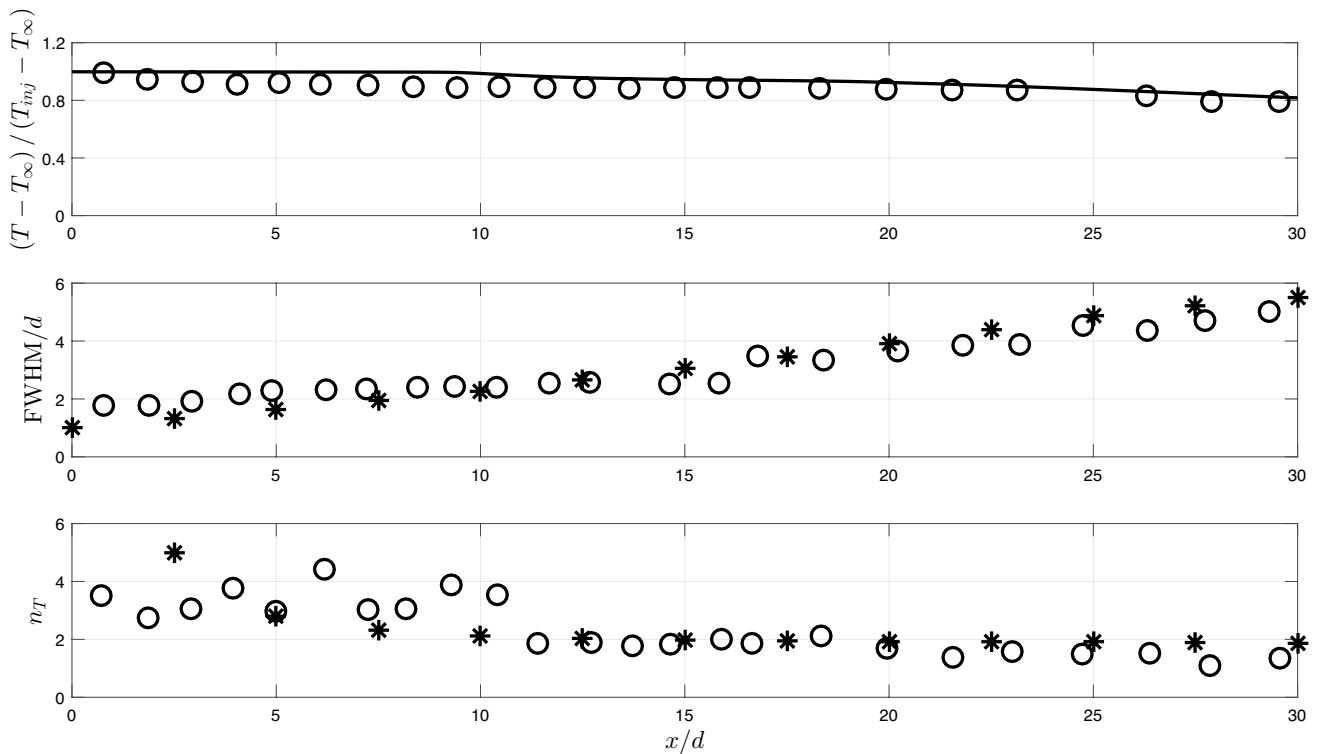


**Fig. 14** Comparison between numerical results and experimental results for case B4 (top: axial temperature distribution; middle: FWHM of temperature; bottom: shape parameter). Lines and star symbols correspond to numerical results, while open circles represent experimental data [20]

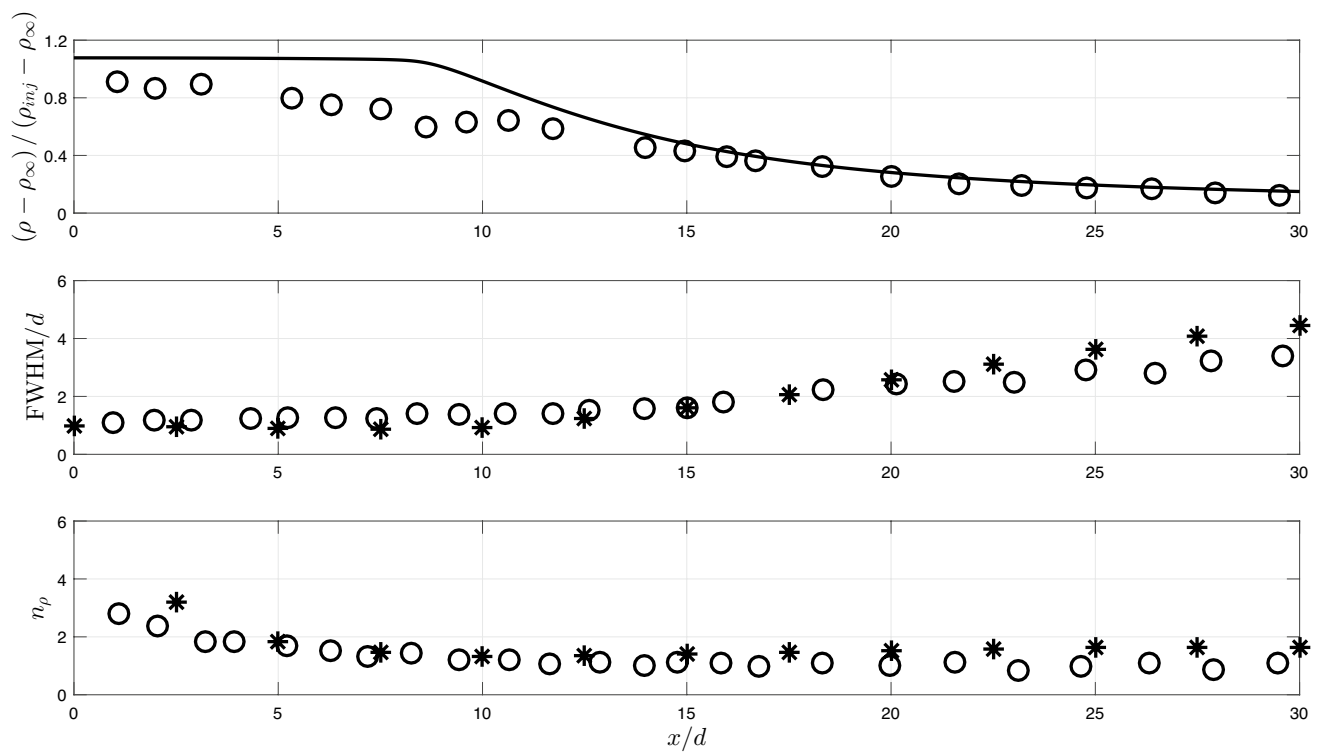


**Fig. 15** Comparison between numerical results and experimental results for case B6 (top: axial density distribution; middle: FWHM of density; bottom: shape parameter). Lines and star symbols correspond to numerical results, while open circles represent experimental data [20]

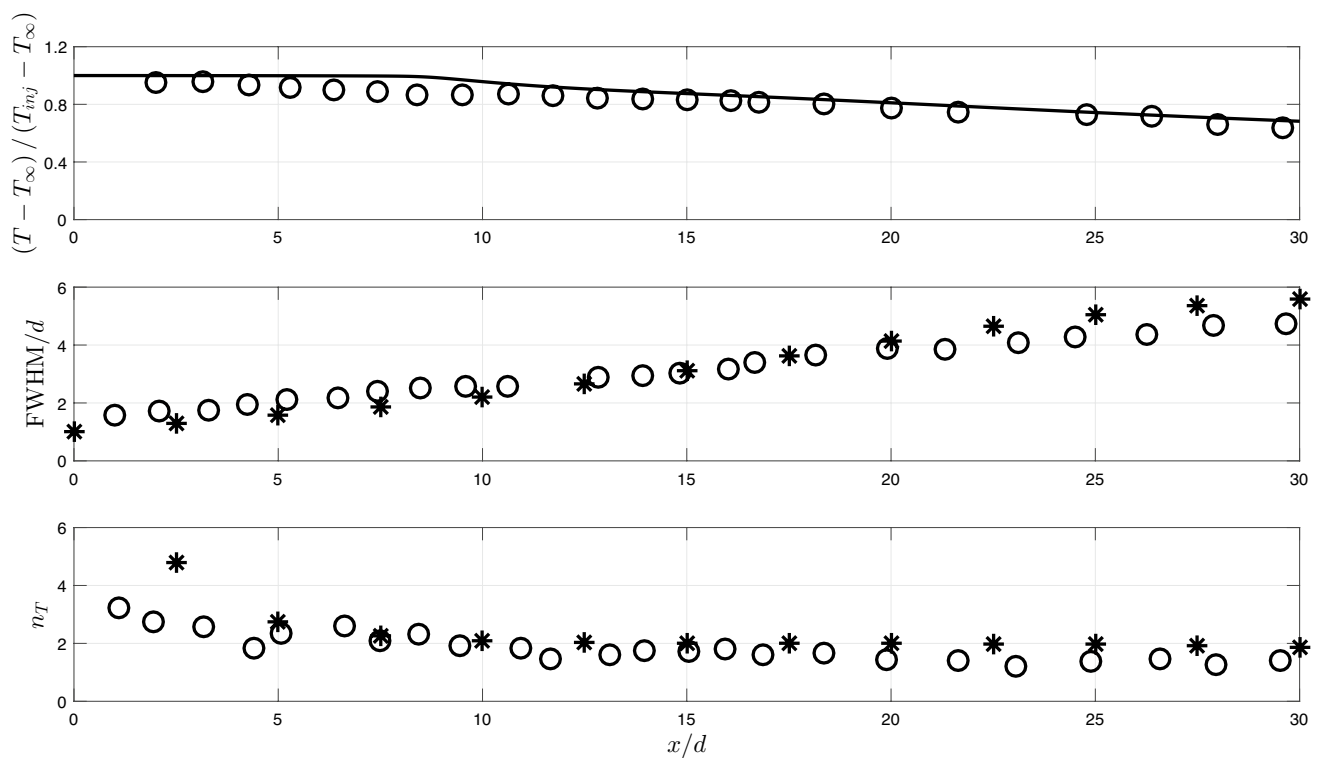


**Fig. 16** Comparison between numerical results and experimental results for case B6 (top: axial temperature distribution; middle: FWHM of temperature; bottom: shape parameter). Lines and star symbols correspond to numerical results, while open circles represent experimental data [20]

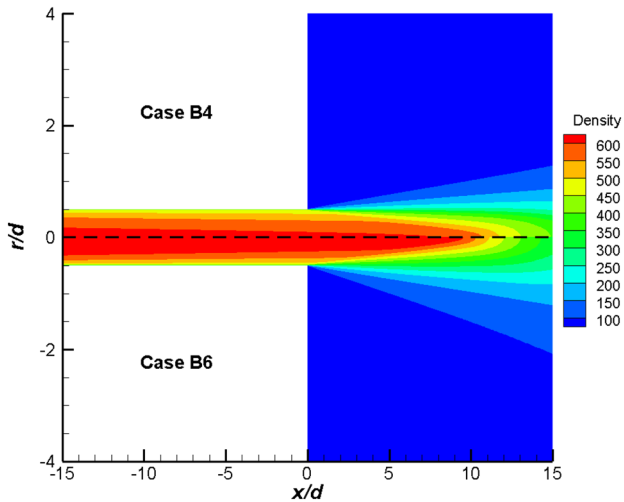


Fig. 17 Comparison of density field between cases B4 and B6

in the 125 K jet after the critical temperature is crossed, the pockets of liquid-like nitrogen start to break from the jet sooner ( $x/d \approx 14$ ) than for the 118 K one at  $x/d \approx 18$ . On the other hand, by considering the injection to take place under supercritical conditions ( $T_{inj}=128$  K), it is possible to observe the characteristic feature of a mixture under liquid-like conditions, with the formation of a dense potential core replacing the slow rate of decay of the axial density until  $x/d \approx 9.8$ , registered for the transcritical injection conditions. The core formation is related to the effect of pseudo-boiling and the eventual transition across the Widom line into supercritical gas-like conditions.

Considering a lower injection temperature (100 K), and a greater injection velocity ( $20 \text{ m s}^{-1}$ ), the axial density decay of case C4 is retrieved in Fig. 19 and the axial temperature evolution in Fig. 20. Here, it is possible to

observe an experimental region of minor density variation until  $x/d \approx 2$ , which numerically extends to  $x/d \approx 9$ . This potential core is formed in the transcritical portion of the jet, which for cases C4 and C6 correspond to a value of  $\rho^* = 0.8677$ . After the critical temperature is crossed, the liquid-like nitrogen jet will continue to develop until entrained by chamber fluid, until breaking.

Increasing the pressure from 4 MPa in case C4 to 6 MPa in case C6, several differences can be observed. Figures 21 and 22 the same initial numerical dense core registered for case C4. However, the experimental data no longer displays the same initial region of relatively constant density. Further away from the critical pressure of nitrogen, it is possible to observe a closer agreement with the experimental data, starting from  $x/d$  of about 15, where the conditions in the chamber start to dominate over the jet evolution.

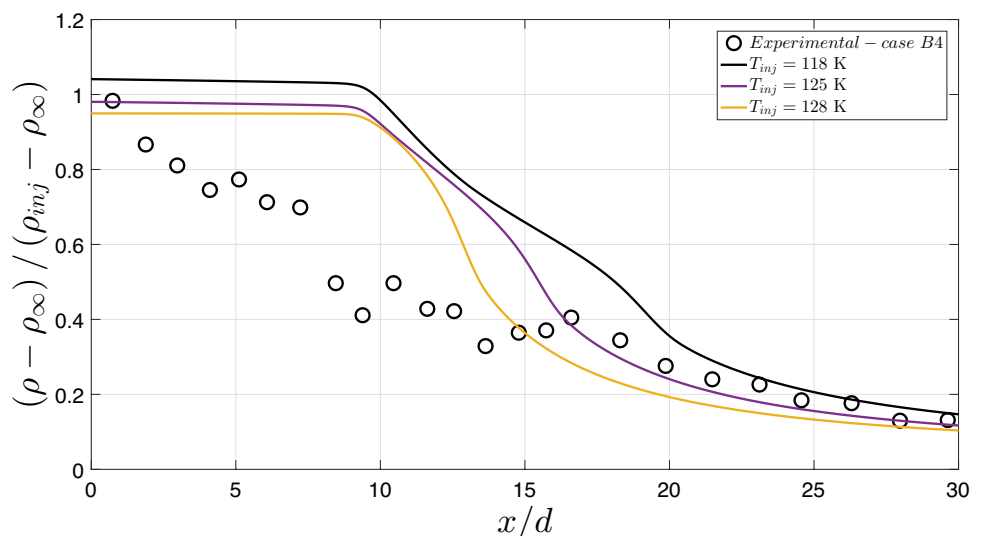
As depicted in Fig. 23, comparing the density fields of cases C4 and C6, the heat transfer exchange between the injector walls and the transcritical jets is not sufficient to reach the jet centerline and influence the axial evolution of density, to result in the formation of a dense potential core, leading to minor differences on the jet inside the chamber.

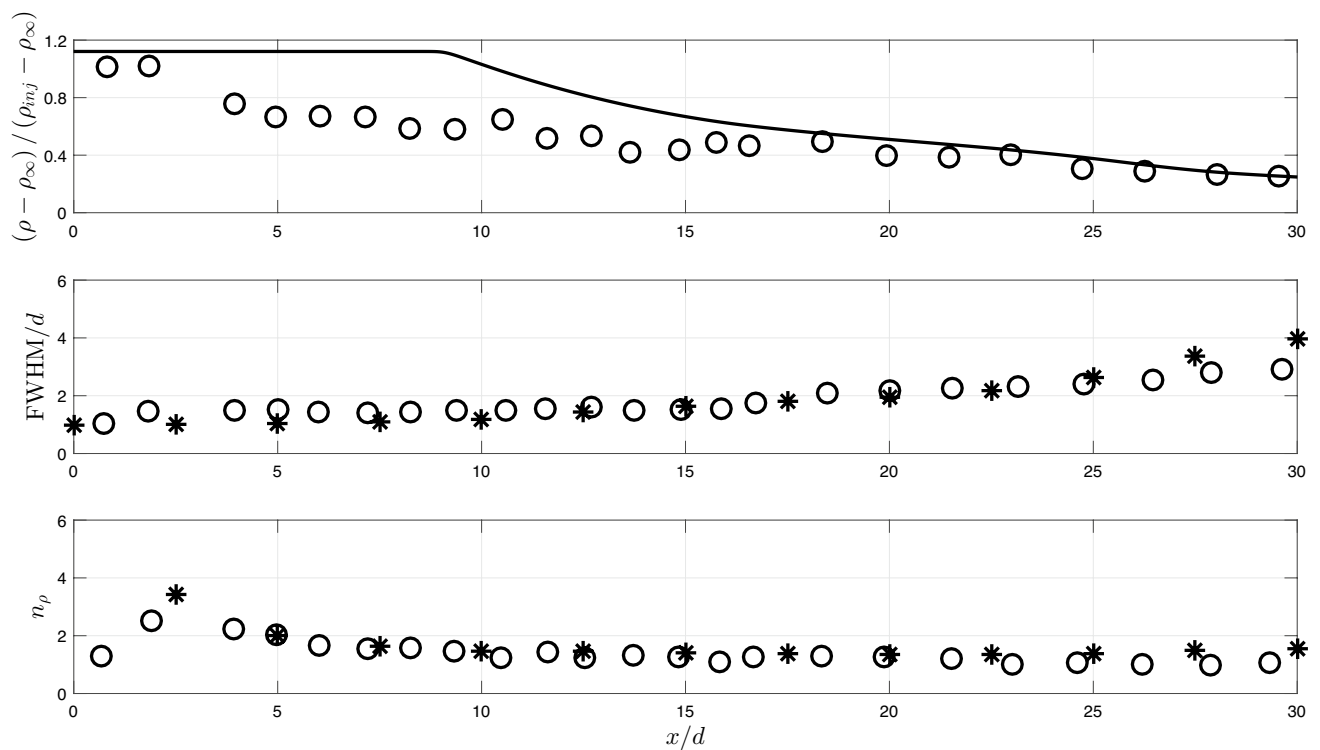
While differences between the experiments and the numerical predictions are observed for cases B and C in terms of the axial density decay rate, the proposed incompressible but variable density approach can predict the jet spreading rates in terms of density and temperature for all experimental test cases, showcasing the ability of the

Table 4 Reduced temperature corresponding to the selected injection temperatures for case B4

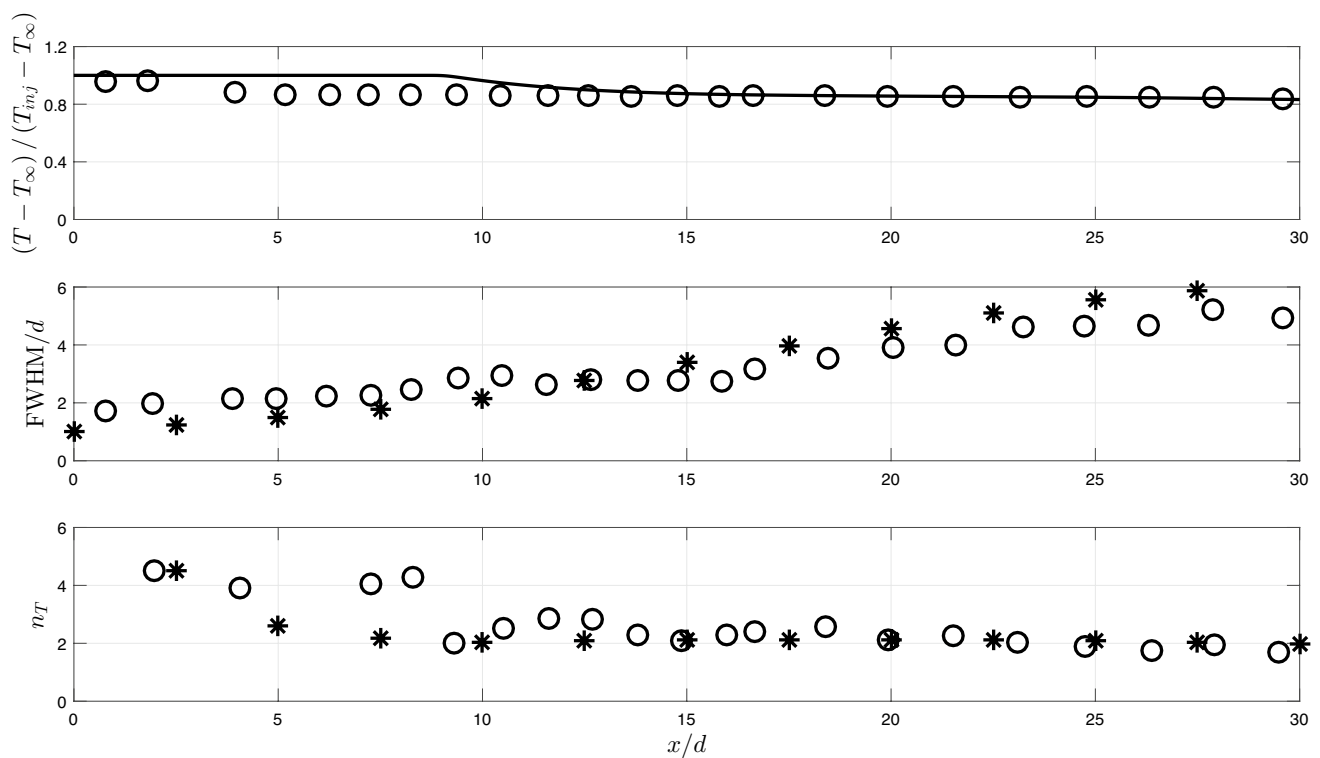
$T_{inj}$ [K]	$T_r$
118	0.94
125	0.99
128	1.01

Fig. 18 Axial density distribution for case B4





**Fig. 19** Comparison between numerical results and experimental results for case C4 (top: axial density distribution; middle: FWHM of density; bottom: shape parameter). Lines and star symbols correspond to numerical results, while open circles represent experimental data [20]



**Fig. 20** Comparison between numerical results and experimental results for case C4 (top: axial temperature distribution; middle: FWHM of temperature; bottom: shape parameter). Lines and star symbols correspond to numerical results, while open circles represent experimental data [20]

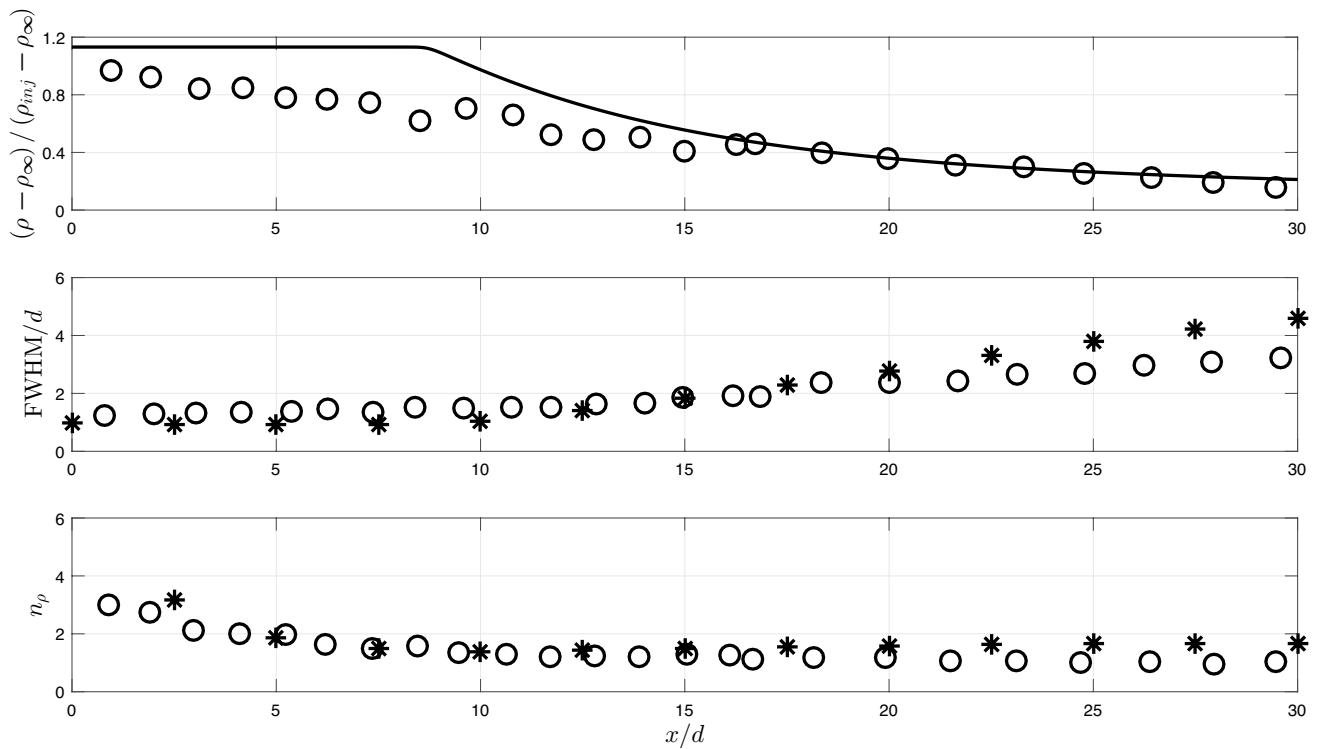


**Fig. 21** Comparison between numerical results and experimental results for case C6 (top: axial density distribution; middle: FWHM of density; bottom: shape parameter). Lines and star symbols correspond to numerical results, while open circles represent experimental data [20]

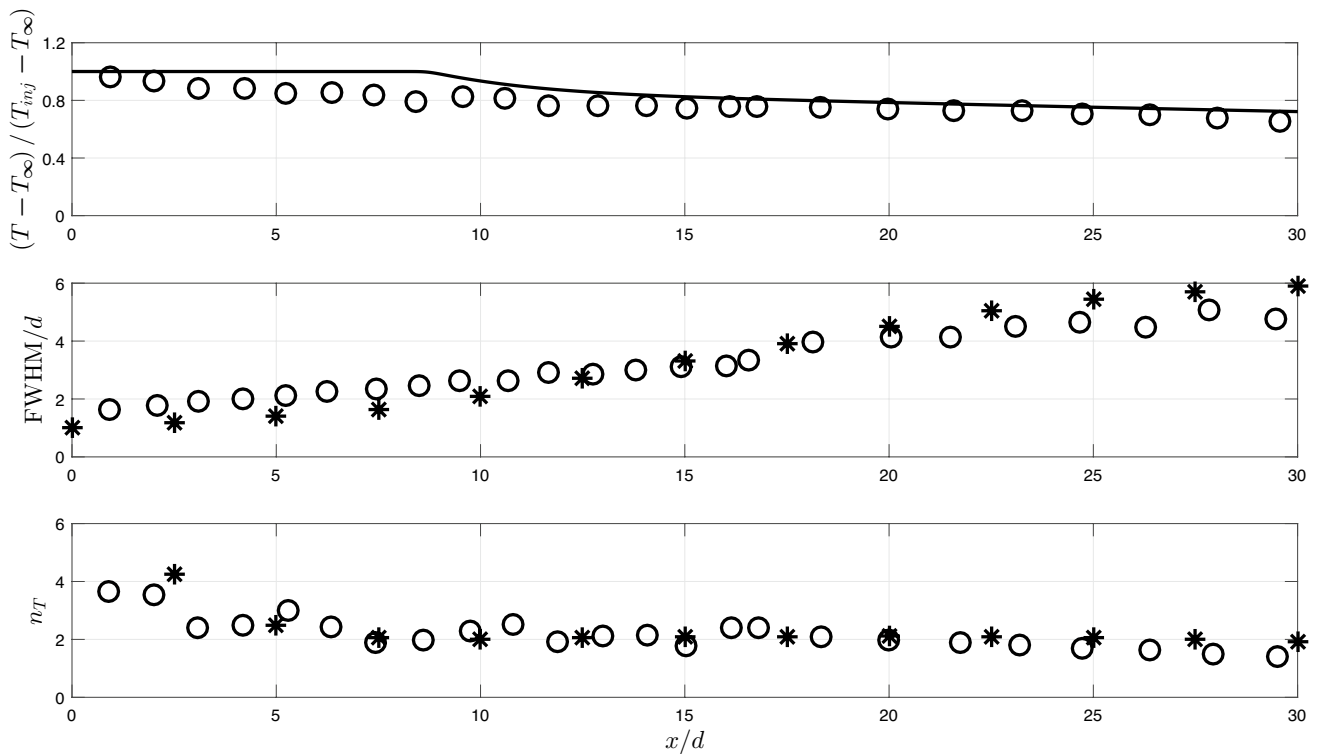


**Fig. 22** Comparison between numerical results and experimental results for case C6 (top: axial temperature distribution; middle: FWHM of temperature; bottom: shape parameter). Lines and star symbols correspond to numerical results, while open circles represent experimental data [20]



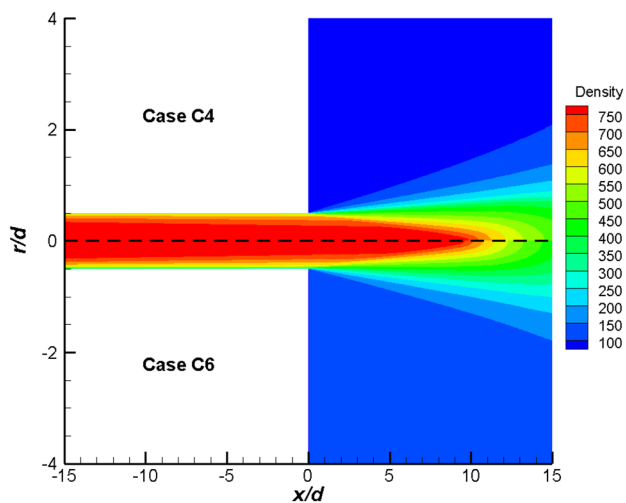


**Fig. 23** Comparison of density field between cases C4 and C6

incompressible but variable density approach in replicating turbulent mixing and account for the real gas effects. The ability to predict transcritical behavior through compressible or incompressible but variable density formulations lies with including phase separation into the models to account for the possible formation of multiphase flow. Moreover, the experiments put forth by Oswald and Schik [20] rely on a highly complex Raman spectroscopy experimental setup [51] where it is explained that the experimental transcritical jet configurations can be under-predicted. Accordingly, Oswald and Schik [20] report a value of 30% for cases C4 and C6. On the other hand, the assumption of a constant Raman cross-section does not affect the supercritical jets (A4 and A6). Moreover, Oswald and Schik [20] point out that only the absolute density values are affected by the constant Raman cross-section, which means that the FWHM and the shape parameters for density and temperature are not affected by this issue.

Lastly, the shape parameters for density and temperature indicate that no self-similar state is reached since the parameters always exhibit values higher than one.

## 6 Conclusion

This manuscript extends the heat transfer injector effect to nitrogen injection at transcritical conditions into a quiescent environment. In addition to assessing axial density decay, jet spreading rates in terms of density and temperature are also looked into, which serve as a measure of mixing efficiency. These indicate that heat propagation is dominant over momentum transport. Moreover, the formation of the previously identified and computed transitional supercritical regime is hypothesized to be derived from the low injection

velocities. Good confidence is obtained from the results, indicating that phase separation occurs at transcritical injection conditions. Surface tension and interface formation may have a role in this plethora of highly coupled phenomena.

The results seem to be in line with previous literature regarding mechanical and thermal breakup jet mechanisms. In light of these results, it seems reasonable to consider the pseudo-critical point as denoting a fundamental change in jet behavior instead of the critical point. Lastly, the influence of these two mechanisms in the potential core length directly impacts the operation of liquid rocket engines, in regards to the development of combustion instabilities.

**Acknowledgements** The present work was performed under the scope of activities at the Aeronautics and Astronautics Research Center (AEROG) of the Laboratório Associado em Energia, Transportes e Aeronáutica (LAETA), and was supported by the Fundação para a Ciência e Tecnologia (Grant No. SFRH/BD/136381/2018, Project No. UIDB/50022/2020, UIDP/50022/2020 and LA/P/0079/2020).

**Funding** Open access funding provided by FCTIFCCN (b-on).

**Data availability** The data presented in this study are available on request from the corresponding author.

**Conflict of interest** The authors declare that they have no conflict of interest.

**Open Access** This article is licensed under a Creative Commons Attribution 4.0 International License, which permits use, sharing, adaptation, distribution and reproduction in any medium or format, as long as you give appropriate credit to the original author(s) and the source, provide a link to the Creative Commons licence, and indicate if changes were made. The images or other third party material in this article are included in the article's Creative Commons licence, unless indicated otherwise in a credit line to the material. If material is not included in the article's Creative Commons licence and your intended use is not permitted by statutory regulation or exceeds the permitted use, you will need to obtain permission directly from the copyright holder. To view a copy of this licence, visit <http://creativecommons.org/licenses/by/4.0/>.

## References

- Oswald, M., Smith, J.J., Braman, R., Hussong, J., Schik, A., Chehroudi, B., Talley, D.G.: Injection of Fluids into Supercritical Environments. *Combust. Sci. Technol.* **178**(1–3), 49–100 (2006). <https://doi.org/10.1080/00102200500292464>
- Smith, J.J., Schneider, G., Suslov, D., Oswald, M., Haidn, O.: Steady-state high pressure LOx/H2 rocket engine combustion. *Aerosp. Sci. Technol.* **11**(1), 39–47 (2007). <https://doi.org/10.1016/j.ast.2006.08.007>
- Masquelet, M., Menon, S., Jin, Y., Friedrich, R.: Simulation of unsteady combustion in a LOX-GH2 fueled rocket engine. *Aerosp. Sci. Technol.* **13**(8), 466–474 (2009). <https://doi.org/10.1016/j.ast.2009.07.005>
- Ahn, K., Kim, J., Choi, H.: Effects of injector recess on heat Flux in a combustion chamber with cooling channels. *Aerosp. Sci. Technol.* **37**, 110–116 (2014). <https://doi.org/10.1016/j.ast.2014.05.012>
- Cho, S., Kim, H., Yoon, Y., Sung, H.: Dynamic characteristics of a cryogenic Swirl flow under supercritical conditions. *Aerosp. Sci.*

- Technol. **51**, 162–170 (2016). <https://doi.org/10.1016/j.ast.2016.02.008>
6. Kang, J., Heo, J., Sung, H., Yoon, Y.: Dynamic characteristics of a cryogenic nitrogen Swirl injector under supercritical conditions. *Aerosp. Sci. Technol.* **67**, 398–411 (2017). <https://doi.org/10.1016/j.ast.2017.04.010>
  7. Li, H., Ye, L., Wei, X., Li, T., Li, S.: The design and main performance of a hydrogen peroxide/kerosene coaxial-swirl injector in a lab-scale rocket engine. *Aerosp. Sci. Technol.* **70**, 636–643 (2017). <https://doi.org/10.1016/j.ast.2017.09.003>
  8. Gascoïn, N., Gillard, P., Bouchez, M.: Chemical composition and mass flow measurements in a supercritical reactive flow for hypersonic real-time Application. *Aerosp. Sci. Technol.* **14**(4), 266–275 (2010). <https://doi.org/10.1016/j.ast.2010.01.007>
  9. Shokri, M., Ebrahimi, A.: Heat transfer aspects of regenerative-cooling in methane-based propulsion systems. *Aerosp. Sci. Technol.* **82–83**, 412–424 (2018). <https://doi.org/10.1016/j.ast.2018.09.025>
  10. Sun, F., Li, X., Boetcher, S.K.S., Xie, G.: Inhomogeneous behavior of supercritical hydrocarbon fuel flow in a regenerative cooling channel for a Scramjet Engine. *Aerosp. Sci. Technol.* **117**, 106901 (2021). <https://doi.org/10.1016/j.ast.2021.106901>
  11. Perakis, N., Preis, L., Haidn, O.J.: Wall heat flux evaluation in regeneratively cooled rocket thrust chambers. *J. Thermophys. Heat Transfer* **35**(1), 127–141 (2021). <https://doi.org/10.2514/1.T6056>
  12. Raju, M., Banuti, D.T., Ma, P.C., Ihme, M.: Widom lines in binary mixtures of supercritical fluids. *Sci. Rep.* (2017). <https://doi.org/10.1038/s41598-017-03334-3>
  13. Gerber, V., Baab, S., Förster, F.J., Mandler, H., Weigand, B., Lamanna, G.: Fluid injection with supercritical reservoir conditions: overview on morphology and mixing. *J. Supercritical Fluids* **169**, 105097 (2021). <https://doi.org/10.1016/j.supflu.2020.105097>
  14. Banuti, D.T.: Crossing the Widom-line – Supercritical Pseudo-boiling. *J. Supercrit. Fluids* **98**, 12–16 (2015). <https://doi.org/10.1016/j.supflu.2014.12.019>
  15. Banuti, D.T., Hannemann, K.: The absence of a dense potential core in supercritical injection: a thermal break-up mechanism. *Phys. Fluids* **28**(3), 035103 (2016). <https://doi.org/10.1063/1.4943038>
  16. Lapenna, P.E., Creta, F.: Mixing under transcritical conditions: an a-priori study using direct numerical simulation. *J. Supercrit. Fluids* **128**, 263–278 (2017). <https://doi.org/10.1016/j.supflu.2017.05.005>
  17. Magalhães, L.B., Silva, A.R.R., Barata, J.M.M.: Contribution to the Physical description of supercritical cold flow injection: the case of nitrogen. *Acta Astronaut.* **190**, 251–260 (2022)
  18. Banuti, D.T., Raju, M., Ma, C., Ihme, M., Hickey, J.: Seven Questions about Supercritical Fluids – Towards a New Fluid State Diagram. In: 55th AIAA Aerospace Sciences Meeting (2017). 10.2514/6.2017-1106
  19. Oschwald, M., Schik, A., Klar, M., Mayer, W.: Investigation Of Coaxial LN<sub>2</sub>/GH<sub>2</sub>-injection at Supercritical Pressure by Spontaneous Raman Scattering. In: 35th Joint Propulsion Conference and Exhibit (1999). 10.2514/6.1999-2887
  20. Oschwald, M., Schik, A.: Supercritical nitrogen free jet investigated by spontaneous Raman scattering. *Exp. Fluids* **27**(6), 497–506 (1999). <https://doi.org/10.2514/6.1999-2887>
  21. Mayer, W., Telaar, J., Branam, R., Schneider, G., Hussong, J.: Raman measurements of cryogenic injection at supercritical pressure. *Heat Mass Transf.* **39**(8–9), 709–719 (2003). <https://doi.org/10.1007/s00231-002-0315-x>
  22. Dahms, R.N., Manin, J., Pickett, L.M., Oefelein, J.C.: Understanding high-pressure gas-liquid interface phenomena in diesel engines. *Proc. Combust. Inst.* **34**(1), 1667–1675 (2013). <https://doi.org/10.1016/j.proci.2012.06.169>
  23. de Risi, A., Donato, T., Laforgia, D.: Theoretical investigation on variable-density sprays. *Atom. Sprays* **12**(1–3), 329–358 (2002). <https://doi.org/10.1615/AtomizSpr.v12.i123.170>
  24. Kim, N., Kim, Y.: Large eddy simulation based multi-environment PDF modelling for mixing processes of transcritical and supercritical cryogenic nitrogen jets. *Cryogenics* **110**, 103134 (2020). <https://doi.org/10.1016/j.cryogenics.2020.103134>
  25. Barata, J., Gökalp, I., Silva, A.: Numerical study of cryogenic jets under supercritical conditions. *J. Propul. Power* **19**(1), 142–147 (2003). <https://doi.org/10.2514/2.6090>
  26. Chehroudi, B., Talley, D., Coy, E.: Initial Growth Rate and Visual Characteristics of a Round Jet Into a Sub- to Supercritical Environment of Relevance to Rocket, Gas Turbine, and Diesel Engines. In: 37th Aerospace Sciences Meeting and Exhibit (1999). 10.2514/6.1999-206
  27. Lacaze, G., Schmitt, T., Ruiz, A., Oefelein, J.C.: Comparison of energy-, pressure- and enthalpy-based approaches for modeling supercritical flows. *Comput. Fluids* **181**, 35–56 (2019). <https://doi.org/10.1016/j.compfluid.2019.01.002>
  28. Segal, C., Polikhov, S.A.: Subcritical to supercritical mixing. *Phys. Fluids* **20**(5), 052101 (2008). <https://doi.org/10.1063/1.2912055>
  29. Jofre, L., Urzay, J.: Transcritical diffuse-interface hydrodynamics of propellants in high-pressure combustors of chemical propulsion systems. *Prog. Energy Combust. Sci.* **82**, 100877 (2021). <https://doi.org/10.1016/j.pecs.2020.100877>
  30. Ries, F., Sadiki, A.: Supercritical and transcritical turbulent injection processes: consistency of numerical modeling. *Atom. Sprays* **31**(5), 37–71 (2021). <https://doi.org/10.1615/AtomizSpr.2021035399>
  31. Meng, H., Yang, V.: A unified treatment of general fluid thermodynamics and its application to a preconditioning scheme. *J. Comput. Phys.* **189**(1), 277–304 (2003). [https://doi.org/10.1016/S0021-9991\(03\)00211-0](https://doi.org/10.1016/S0021-9991(03)00211-0)
  32. Sierra-Pallares, J., Santiago-Casado, P., Castro, F.: Numerical modelling of supercritical submerged water jets in a subcritical co-flow. *J. Supercrit. Fluids* **65**, 45–53 (2012). <https://doi.org/10.1016/j.supflu.2012.02.028>
  33. Tao, Z., Cheng, Z., Zhu, J., Hu, X., Wang, L.: Correction of low-Reynolds number turbulence model to hydrocarbon fuel at supercritical pressure. *Aerosp. Sci. Technol.* **77**, 156–167 (2018). <https://doi.org/10.1016/j.ast.2018.02.038>
  34. Magalhães, L.B.: Contribution to the Physical Understanding of Supercritical Fluid Flows: A Computational Perspective. PhD thesis, University of Beira Interior (2022)
  35. Launder, B.E., Spalding, D.B.: Lectures in mathematical models of turbulence. Academic Press, London, England (1972)
  36. Magalhães, L., Carvalho, F., Silva, A., Barata, J.: Turbulence modeling insights into supercritical nitrogen mixing layers. *Energies* **13**(7), 1586 (2020)
  37. Petit, X., Ribert, G., Lartigue, G., Domingo, P.: Large eddy simulation of supercritical fluid injection. *J. Supercrit. Fluids* **84**, 61–73 (2013). <https://doi.org/10.1016/j.supflu.2013.09.011>
  38. Peng, D., Robinson, D.B.: A new two-constant equation of state. *Ind. Eng. Chem. Fundam.* **15**(1), 59–64 (1976). <https://doi.org/10.1021/i160057a011>
  39. Ghanbari, M., Ahmadi, M., Lashanizadegan, A.: A comparison between Peng-Robinson and Soave-Redlich-Kwong cubic equations of State from modification perspective. *Cryogenics* **84**, 13–19 (2017). <https://doi.org/10.1002/ghg.1322>
  40. McBride, B.J., Zehe, M.J., Gordon, S.: NASA Glenn Coefficients for Calculating Thermodynamic Properties of Individual

- Species. Technical Report NASA/TP–2002-211556, NASA Glenn Research Center (2002)
41. Lemmon, E.W., Jacobsen, R.T.: Viscosity and thermal conductivity equations for nitrogen, oxygen, argon and air. *Int. J. Thermophys.* **25**(1), 21–69 (2004). <https://doi.org/10.1023/B:IJOT.0000022327.04529.f3>
  42. Leonard, B.P.: A stable and accurate convective modelling procedure based on quadratic upstream interpolation. *Comput. Methods Appl. Mech. Eng.* (1979). [https://doi.org/10.1016/0045-7825\(79\)90034-3](https://doi.org/10.1016/0045-7825(79)90034-3)
  43. Jarczyk, M., Pfitzner, M.: Large Eddy Simulation of Supercritical Nitrogen Jets. In: 50th AIAA Aerospace Sciences Meeting (2012). 10.2514/6.2012-1270
  44. Müller, H., Niedermeier, C.A., Jarczyk, M., Pfitzner, M., Hickel, S., Adams, N.A.: Large Eddy simulation of trans- and supercritical injection. *Progress Propuls. Phys.* **8**, 5–24 (2016). <https://doi.org/10.1051/eucass/201608005>
  45. Roache, P.J.: *Verification and Validation in Computational Science and Engineering*. John Wiley & Sons, Albuquerque, New Mexico, ??? (1998)
  46. Branam, R., Telaar, J., Mayer, W.: 2nd International Workshop on Rocket Combustion Modeling: Atomization, Combustion and Heat Transfer held in Lampoldshausen. Edwards Air Force Base, Technical report, Air Force Research Laboratory (2001)
  47. Schlichting, H., Gersten, K.: *Boundary–Layer Theory*. Springer, ??? (2017)
  48. Linstrom, P.J., Mallard, W.G. (eds.): NIST Chemistry WebBook, NIST Standard Reference Database 69. National Institute of Standards and Technology, ??? (1997). 10.18434/t4d303
  49. Chehroudi, B.: Physical hypothesis for the combustion instability in cryogenic Liquid Rocket Engines. *J. Propuls. Power* **26**(6), 1153–1160 (2010). <https://doi.org/10.2514/1.38451>
  50. Traxinger, C., Zips, J., Pfitzner, M.: Single-phase Instability in Non-premixed Flames under Liquid Rocket Engine Relevant Conditions. *J. Propul. Power* **35**(4), 1–15 (2019). <https://doi.org/10.2514/1.B37395>
  51. Wang, C.H., Wright, R.B.: Effect of density on the raman scattering of molecular Fluids I a detailed study of the scattering polarization, intensity, frequency shift, and spectral shape in gaseous N<sub>2</sub>. *J. Chem. Phys.* **59**(4), 1706–1712 (1973). <https://doi.org/10.1063/1.1680252>

**Publisher's Note** Springer Nature remains neutral with regard to jurisdictional claims in published maps and institutional affiliations.